PHYSICAL REVIEW E VOLUME 55, NUMBER 1 JANUARY 1997

Phase transitions in a confined quasi-two-dimensional colloid suspension

Andrew H. Marcus and Stuart A. Rice
The James Franck Institute, The University of Chicago, Chicago, Illinois 60637

(Received 27 June 1996)

We have used digital video microscopy to study the equilibrium structure of quasi-two-dimensional suspensions of sterically stabilized uncharged polymethylmethacrylate spheres. The spheres are confined between the surfaces of a very thin glass cell. Our experiments reveal the existence of an equilibrium hexatic phase as well as strongly first order liquid-to-hexatic and hexatic-to-solid phase transitions. These observations are in agreement with the predictions of Bladon and Frenkel [Phys. Rev. Lett. **74**, 2519 (1995)] for a confined colloid suspension in which the pair interaction potential between particles has a hard core, and either a very short-range attraction or a very short-range step repulsion. [S1063-651X(97)01901-6]

PACS number(s): 82.70.−y

I. INTRODUCTION

From the point of view of everyday experience, one of the most commonly observed phase transitions is the melting of a solid to form a liquid. In our three-dimensional world this transition from the solid to the liquid phase is characterized by discontinuous changes in density, enthalpy, and entropy. In the language of thermodynamics, the solid becomes unstable with respect to the liquid when the chemical potential of the latter becomes more negative than that of the former; the melting temperature and pressure are determined by the condition that the chemical potentials of the two phases be equal when the phases coexist at equilibrium. It is very important to note that for a first order transition such as melting this thermodynamic instability occurs before any mechanical instability of the solid arises, i.e., there is no mechanical response function of the solid whose frequency continuously decreases with temperature, and which reaches zero at the melting point. On the other hand, in a continuous transition between two crystalline forms of a solid, e.g., in the cubic-to-tetragonal transition in $SrTiO_3$, it is found that the temperature and pressure at which the thermodynamic and mechanical instabilities occur do coincide.

More than 20 years ago it was suggested that the character of the melting transition in two dimensions is fundamentally different from that of the melting transition in three dimensions. Two-dimensional melting is of great theoretical interest, because the type of order that distinguishes solid from liquid phases is qualitatively different from that in three dimensions [1]. In the three-dimensional case the density-density correlation function of the ordered solid phase decays, with increasing particle separation, to a nonzero constant value in the limit of infinite separation. This is the characteristic feature of long-range positional order. In the two-dimensional case the density-density correlation function of the solid phase decays to zero algebraically in the limit of infinite separation, which is the characteristic feature of quasi-long-range order. However, in the two-dimensional system there exists a special kind of long-range order called bond orientational order. According to the Kosterlitz-Thouless-Halperin-Nelson-Young (KTHNY) theory [1–5] two-dimensional solids melt via sequential continuous phase transitions. The first transition is from the solid with quasi-long-range positional order and long-range bond orientation order to a phase with short-range positional order and quasi-long-range bond orientational order, the so-called hexatic phase. This transition is driven by the dissociation of bound dislocation pairs in the solid. The second transition transforms the hexatic phase to a liquid phase in which both positional and bond orientational order have short ranges. This transition is driven by the dissociation of individual dislocations to form disclinations. Although it is currently preferred, the transition sequence described is not the only possible mechanism for two-dimensional melting. For example, it is in principle possible for the dislocation unbinding transition to be preempted by grain-boundary-induced melting, as has been suggested by Chui [6]. The most interesting recent development in the theory of two-dimensional melting is a report, by Bladon and Frenkel [7], of the results of simulations of a two-dimensional assembly of particles which interact via a pairwise additive potential consisting of a hard core repulsion and a very narrow square well attraction (or a very narrow step repulsion). When the width of the attractive well is less than 8% of the hard disc diameter, the system supports two ordered solid phases with the same packing symmetry. The coexistence region of the first order solid-solid transition line ends at a critical point, near which critical point density fluctuations render the solid phases unstable with respect to dislocation unbinding, and the system supports a hexatic phase. For the case that the square well width is close to the limiting value for which the low density solid phase becomes unstable, the hexatic region can extend to the melting line. When this occurs the liquid-to-hexatic transition is predicted to be first order while the hexatic-to-solid transition may be either first or second order. The KTHNY theory has been extended, by Chou and Nelson [8], to account for the essential features of the phase diagram found by Bladon and Frenkel.

Given the striking nature of the KTHNY theory predictions, it is not surprising that both experimental and computer simulation studies of two-dimensional melting have focused attention, almost exclusively, on the search for continuous transitions from the solid phase to the hexatic phase and from the hexatic phase to the liquid phase [7–24]. An early computer simulation study of two-dimensional melting in a system with Coulomb interactions [9,10] is con-

1063-651X/97/55(1)/637(20)/$10.00

sistent with the predictions of the KTHNY theory, as is a more recent study of a two-dimensional colloid system with Yukawa interactions [12]. The most recent and most extensive computer simulation of the melting of a two-dimensional system of particles which have an interparticle potential of the r^{-12} form concludes that there are continuous transitions between the solid and hexatic phases and the hexatic and liquid phases, but that the density range in which the hexatic phase is stable is very small [13]. Earlier, less definitive computer simulations of the two-dimensional hard disc system (and of similar systems with short-range repulsive interactions) lead to the conclusion that two-dimensional melting is a first order transition [14].

The extent of experimental testing of the KTHNY predictions concerning the character of two-dimensional melting has been limited by the difficulty of preparing systems which are acceptable representatives of the theoretical model [15]. Typical representatives of two-dimensional systems are monolayers supported on a substrate. In order that a real system behave as if it were two-dimensional it is necessary but not sufficient for the range of in-plane correlations to greatly exceed the range of out-of-plane correlations [16], and that the interactions between the system and its supporting substrate furnish only a weak perturbation to the properties of the system. Nelson and Halperin [3] and Young [4] have shown that a weak incommensurate substrate potential only slightly modifies the character of the solid-to-hexatic transition. Among the interesting changes induced by the potential of an ordered substrate is long-ranged bond orientational order in the hexatic phase, and a washing out of the dislocation→disclination unbinding transition when the substrate has sixfold symmetry. Also, if the two-dimensional solid monolayer has a preferred orientation with respect to the supporting substrate which is not along a substrate symmetry axis, the melting transition is expected to be Ising-like, corresponding to the two equivalent ways of orienting the two-dimensional solid with respect to a substrate symmetry axis. Experimental studies of the melting of ordered electrons supported on the surface of liquid He [14,17–19], and of the melting of an ordered array of charged polystyrene spheres between two plates [20–22], are consistent with many of the predictions of the KTHNY theory, but some deviations are observed in individual studies [23]. A few other experimental studies give results sometimes in accord and sometimes not in accord with the KTHNY theory [24].

This paper reports the results of studies of the structures and phase transitions in a quasi-two-dimensional suspension of uncharged colloidal spheres in a very thin cell. The particular system we have studied consists of 0.928-μm-diameter spheres of poly(methylmethacrylate) (PMMA) in a cell with wall spacing $\sim$1.2 μm. The surface of each PMMA particle was covered with a $\sim$300-Å oligomeric brush of poly(12-hydroxystearic acid) that acts to stabilize it sterically with respect to aggregation induced by van der Waals forces. We find that the solid phase undergoes a first order transition to a hexatic phase, which subsequently undergoes a first order transition to the liquid phase. These observations are in agreement with the results of the simulations of Bladon and Frenkel for an assembly of particles which interact via a pairwise additive potential consisting of a hard core repulsion and a very narrow square well attraction (or a very narrow step repulsion). We argue in Sec. VI that in the system we studied the interaction between the polymer brushes coating the spherical colloid particles provides the necessary short-range attraction in a small range of interparticle separation where the brushes just begin to interpenetrate.

II. EXPERIMENTAL METHODS AND CONSIDERATIONS

The procedure used to prepare monolayer colloidal suspensions and to construct the experimental glass cells was described in our previous paper [25]. Details specific to the work reported in this paper are given below. Monodisperse PMMA spheres were prepared according to the method of Antl *et al.* [26]. The diameter of the PMMA particles was determined to be σ=0.928 μm by scanning electron microscopy. These measurements also confirmed that the particle size distribution was monodisperse to within 1%. The surface of each particle was covered with a $\sim$300-Å oligomeric brush of poly(3-hydroxystearate) that acts to sterically stabilize it with respect to aggregation induced by van der Waals forces. The PMMA particles were suspended in an aqueous sucrose solution (10% by weight) to eliminate sedimentation, and confined between the walls of a thin glass cell. The cell walls were coated with trihydroxyoctadecylsilane (Huls-Petrarch), which acts to prevent adsorption of PMMA particles to the walls. The spacing between the cell walls could be varied and, for the experiments reported, was set to approximately 1.2 particle diameters ($\sim$1.2 μm). This thin cell configuration constrains the PMMA particle centers to a plane within a small fraction of a particle diameter; we determined by direct microscopic examination that the PMMA particle centers were coplanar to within the depth of focus of the objective ($\sim$0.1 μm). When the wall separation was smaller than $\sim$1.2 μm the particles were observed to be immobilized in the plane; when the wall separation was larger than $\sim$1.2 μm the particles were observed to have out-of-plane motion. No pathological effects were observed when the cell wall spacing was set to $\sim$1.2 μm. The properties of these geometrically confined suspensions were studied over the reduced two-dimensional density range $\rho^*=\rho\sigma^2=0.01$–0.93.

The digital video microscopy (DVM) measurements were made using an Olympus BH3 metallurgical microscope with a 100×, numerical aperture 1.2, oil immersion objective. As already noted, the objective's depth of focus is a fraction of the PMMA sphere diameter, so that nonplanar particle configurations were easily detected. Images of the suspension were captured using an Hitachi charge-coupled device (CCD) video camera mounted to the camera eyepiece. The frame frequency of the CCD camera was 30 Hz, while its shutter speed was one-one-hundreth of a second. The analog camera output was sent directly to the video port of a Silicon Graphics (SGI) Indy workstation. The SGI frame grabber supplied with the workstation was used to digitize sequences of 320×240 (and in some cases, 640×480) square pixel frames. A typical run consisted of 100 frames in sequence, corresponding to roughly 25 Mbyte of data in the case of 320×240 size images. All image processing procedures were implemented using IDL (Research Systems, Inc.), a programming language optimized for visual data analysis. The pixel length was calibrated by imaging a transmission electron microscope (TEM) grid of known scale. The aspect ratio was determined to be 1±0.1 and the calibrated pixel dimension was 1 pixel=0.174±0.0015 μm for 320×240 size images and 1 pixel=0.177±0.0015 μm for 640×480 size images.

A detailed description of the precision with which particle position can be measured in these experiments can be found in our previous paper. Briefly, the center-of-mass positions were determined with 0.1 pixel precision; for the 320×240 square pixel images the precision of center-of-mass location was 17.4 nm, while for the 640×480 square pixel images it was 17.7 nm. This precision of the particle location is sufficient to calculate the mean particle density (using the number of particles in the frame and the pixel-to-length calibration) and the spatial correlation functions with much greater accuracy than is reported in any of our tables.

The observable in the DVM experiment is a complete set of two-dimensional N particle trajectories, which can be combined to define the time-dependent density

$$\rho(\mathbf{r},t)=\sum_{i=1}^{N} \delta(\mathbf{r}-\mathbf{r}_i(t)). \tag{2.1}$$

The process of transforming the information contained in a sequence of digitized images into the time-dependent density profile described by Eq. (2.1) is discussed in our previous paper [25]. A more detailed description is given in an article by Crocker and Grier [27]. Given the trajectory data it is a straightforward, though numerically taxing, application of statistical mechanics to calculate either static or dynamic spatial correlation functions of interest. For the structural studies presented in this work, only static quantities are examined.

Two key elements in the study of two-dimensional melting are the establishment of equilibrium and the ability to measure spatial correlation functions of the appropriate order parameters accurately. As noted by Bagchi, Anderson, and Swope [13], in the vicinity of a phase boundary exceedingly large correlation lengths may influence the results of the analysis of any finite-size subsystem presumably in equilibrium with a much larger, although finite, total system. Similarly, long correlation times can lead to bottlenecks during the course of equilibration that cause the system to exist in long-lived metastable states.

The total area of our sample cell is a few square centimeters. The method we have used to adjust the sample cell thickness does not achieve uniform separation of the cell walls over the entire cell, but the portion which is thin enough to constrain the colloid particles to one plane occupies the larger fraction of the total area of the cell. Indeed, in the systems we studied it was possible to prepare monolayer suspensions comprised of over 10^6 particles with a uniform number density. As an example, Fig. 1 shows a wide angle view of an instantaneous configuration at the reduced density $\rho^*=0.83$. In this sample configuration there are 9242 particles in the field of view, while the total system size is effectively infinite. Each sample configuration constitutes a ‘‘subblock’’ of the infinite system. Provided that the subblock size is large compared to the finite translational correlation length, it is possible to measure the functional forms of the translational and bond orientational correlation functions accurately. On the other hand, if the length of the subblock is small or comparable to the translational correlation length, the measured correlation functions must scale with the subblock size. For all the densities we examined, it was found that the functional form of the correlation functions could be accurately determined from subblocks that contain approximately 2000 particles. In Fig. 2 we plot comparisons of bond-orientational and translational correlation functions (defined in Sec. III) based on the ~9000 particle (or 9K) sample shown in Fig. 1 and subblocks made by dividing the field into four equal and equivalent quadrants (~2225 particles, or 2.2K). In all cases, we used periodic boundary conditions for the calculations. The solid curves represent the calculated correlation functions of the 9K samples, while the circles indicate the values corresponding to the 2.2K samples. The differences in subblock size have no effect on the computed correlation functions. Furthermore, the envelope of the translational correlation function decays to unity within 10 μm; the translational correlation length is on the order of a few particle diameters. Thus for our investigations the 2.2K samples are sufficiently large to accurately determine the structural properties of the system. We will discuss Figs. 1 and 2 further in Sec. III. However, it should be noted that for this sample density the translational correlation function is short ranged while the bond-orientational correlations decay algebraically, indicative that the phase observed is hexatic.

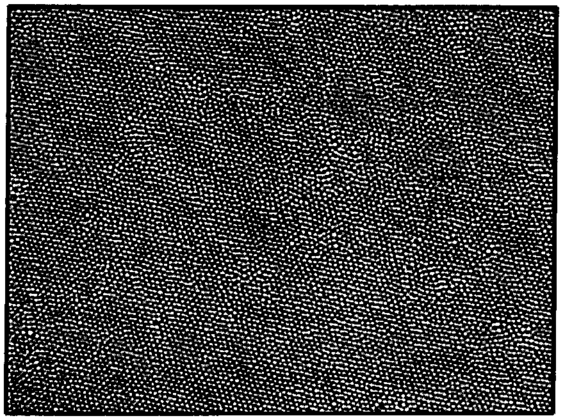

FIG. 1. Wide angle view of a sample quasi-two-dimensional particle configuration with reduced areal density, $\rho^*=0.83$. There are 9248 (~9 K) particles in the field of view; however, approximately 10^6 particles are confined to a single layer in the sample cell. The frame dimension is 113×85 μm^2. Note that the particle density is uniform across the field of view, as it is across the major portion of the sample.

Our concerns about equilibration were addressed by requiring that consistent, reproducible results be achieved while recording data over a 72–168-h period at each sample density. Since the collision time in the highest density systems we studied is approximately 100 ms, this procedure allowed sufficient time for the system to reach equilibrium. Figure 3 shows Voronoi constructions for a sequence of images taken from a 9K particle field with after 72 h of equilibration. Frames A and B are separated by 30 ms, while A and C are separated by 600 ms. Sixfold-coordinated sites are represented as white hexagons, while red and green polygons

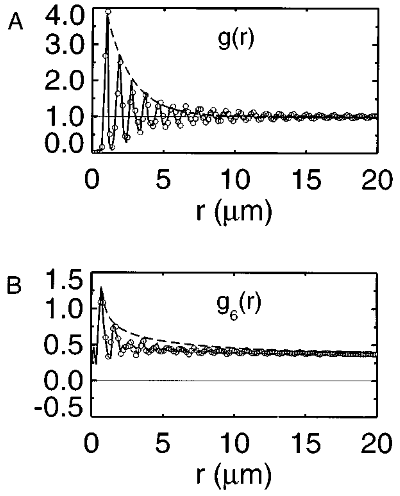

FIG. 2. Size dependence of the translational pair correlation function (A) and the bond orientational pair correlation function (B) based on particle configurations similar to that shown in Fig. 1 ($\rho^*=0.83$). The solid curves are the results of calculations that used the entire ~9K particle field, while the circles correspond to an analysis based on a field 25% this size (~2.25K particles). The dashed curves indicate that the translational pair correlation function is short ranged, and that the correlation in bond orientations is quasi-long-ranged, characteristic of hexatic order (see text, Sec. III).

indicate fivefold and sevenfold coordination, respectively. A site that has a coordination number other than six is called a disclination. In any instantaneous configuration, bound dislocation pairs occur as quartets of alternating fivefold and sevenfold disclinations. Each such configuration typically also shows the presence of unbound ''free'' dislocations made up of individual tightly bound fivefold and sevenfold disclinations. The slow algebraic decay of the bond-orientational order in the hexatic phase is due to the presence of a small steady-state concentration of unbound dislocations. We observe that dislocations and clusters of dislocation defects appear and disappear on the time scale of successive video frames, and that their absolute locations are temporally uncorrelated. This can only be possible if bound dislocations are thermally activated and destroyed on a time scale much shorter than the experimental sampling time interval (30 ms). Furthermore, since free dislocations are seen to appear and disappear between subsequent frames, the pairing, unpairing, and diffusion of free dislocations must occur on time scales shorter than 30 ms. In Sec. IV we will analyze each of these processes in detail and estimate their associated energies. This is a crucial issue in establishing the applicability of the KTHNY theory to the behavior of our particular system [28].

III. BOND ORIENTATIONAL AND TRANSLATIONAL ORDER

Several excellent review articles describing the KTHNY melting theory have been published over the last decade [24]; to place our findings into a proper context we briefly sketch the relevant features of that theory here. The KTHNY theory is based on a description of the solid phase as a deformable elastic medium that is, by definition, characterized by quasi-long-range positional order and long-range bond orientational order. At any temperature greater than zero, such a solid in thermal equilibrium will necessarily have a nonzero density of tightly bound dislocation pairs [29]. The quasi-long-range positional order of the solid phase is destroyed by free dislocations which are generated by dislocation pair unbinding. The concentration of free dislocations increases with increasing temperature until the solid becomes mechanically unstable, at which point there is a continuous transition to the hexatic phase; this transition occurs when the dimensionless combination of elastic constants, K, falls below the numerical value

$$K=\frac{4a_0^2}{k_BT}\,\frac{\mu(\mu+\lambda)}{2\mu+\lambda}=16\pi, \tag{3.1}$$

where μ and λ are the Lamé elastic constants and a_0 is the lattice spacing. As a consequence of the Halperin-Nelson-Young renormalization group analysis of the dislocation pair unbinding transition, the density-density correlation function in the ordered solid phase is predicted to decay algebraically:

$$g_{\mathbf{G}}(r)=\langle\rho_{\mathbf{G}}(0)\rho_{\mathbf{G}}(r)\rangle\propto r^{-\eta}\quad\text{with}\ \tfrac{1}{4}\leqslant\eta\leqslant\tfrac{1}{3}. \tag{3.2}$$

$\mathbf{G}$ is a reciprocal-lattice vector of the solid, and $\rho_{\mathbf{G}}(r)$ are the Fourier components of the singlet particle densities

$$\rho_{\mathbf{G}}(r)=\sum_{i=1}^{N}e^{i\mathbf{G}\cdot\mathbf{r}_i}\delta(r-r_i). \tag{3.3}$$

Equation (3.2) is valid at the first Bragg diffraction peak just below the dislocation pair unbinding transition. This predicted behavior of the density-density correlation function of the solid phase is analogous to that for the Kosterlitz-Thouless vortex unbinding transition in two-dimensional superfluids, superconductors and XY systems [24].

Before the dislocation→disclination unbinding transition occurs, the hexatic phase is anisotropic and the bond orientational correlation function is predicted to exhibit quasi-long-range order,

$$g_6(r)=\frac{\langle\psi_6^*(0)\psi_6(r)\rangle}{\langle\delta(r_i)\delta(r_j-r)\rangle}\propto r^{-\eta_6}\quad\text{with}\ 0\leqslant\eta_6\leqslant\tfrac{1}{4} \tag{3.4}$$

and

$$\psi_6(r_i)=\left\langle\frac{1}{N}\sum_j e^{6i\theta(r_{ij})}\right\rangle. \tag{3.5}$$

In Eq. (3.5), $\psi_6(r_i)$ is the local bond orientational order parameter, where the index j counts the ith particle's nearest neighbors, $\theta(r_{ij})$ is the angle between the bond connecting particles i and j and an arbitrary fixed reference axis, and N is the number of i-j bonds. Similarly, in Eq. (3.4) the index i runs over all particles, and j counts the ith particles nearest neighbors. Although the translational order is destroyed by a small population of free dislocations, these defects have much less effect on the bond orientational order. Strandburg [24] pointed out that because the bond orientational correlation function of the hexatic phase decays to zero, albeit slowly, the static structure function should be isotropic in the

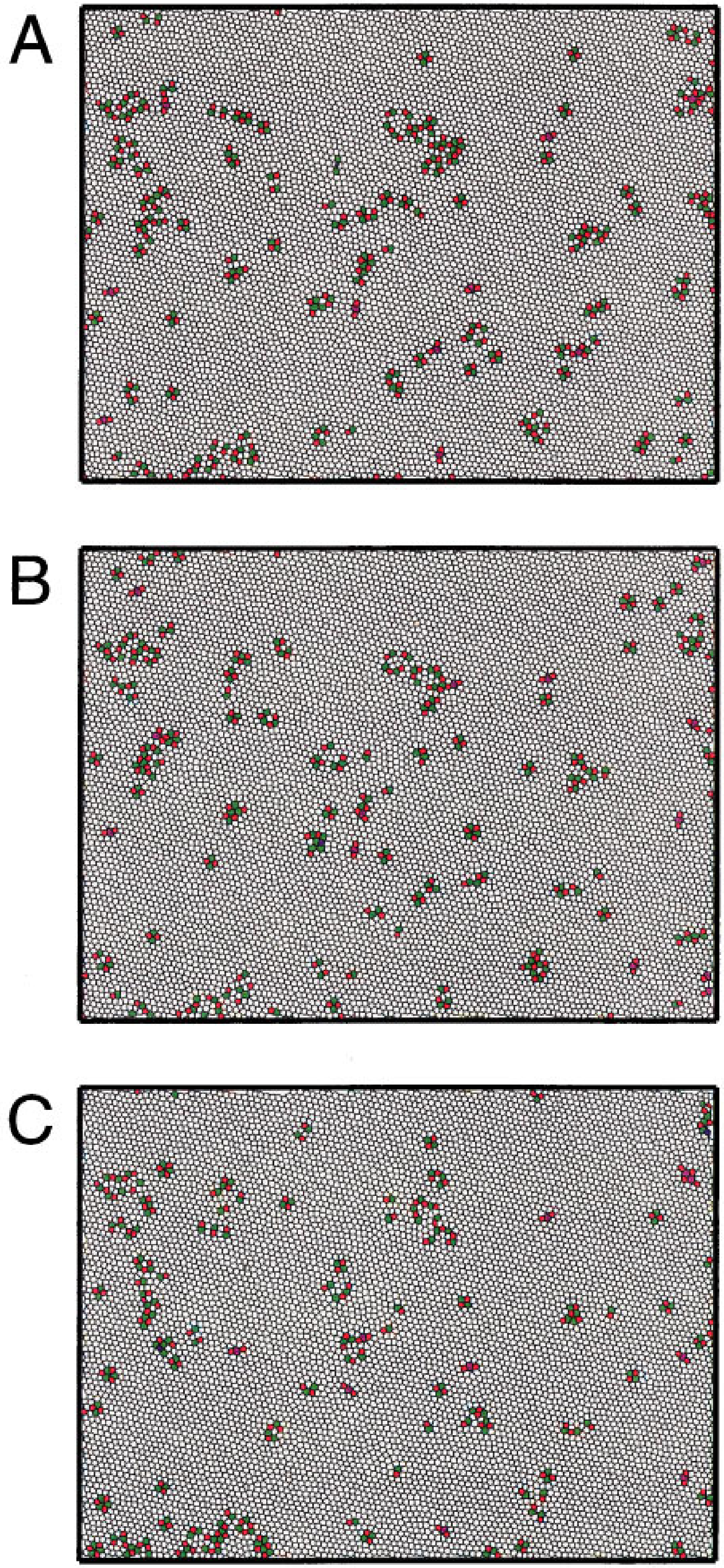

FIG. 3. Voronoi constructions for a sequence of particle configurations with $N\sim 9$ K and $\rho^{*}=0.83$. Frames A and B are separated by 33 ms, while frames A and C are separated by 660 ms. The color coding is as follows. Sixfold-coordinated sites are white, fivefold sites are red, sevenfold sites are filled green, fourfold sites are blue, and eightfold sites are purple. Defects of all morphologies appear and disappear on the same time scale as successive video frames.

TABLE I. Experimental samples. The frame area A is 320×240 pix^2 (2219.5 μm^2). The areal density is measured in units of particle number per frame area normalized by the particle diameter ($N\sigma^2/A$).

Number of particles inside field of view		Scattering pattern [as exhibited by $S(k)$]	Thermodynamic state
28	0.011	isotropic	dilute liquid
198	0.077	isotropic	dilute liquid
622	0.241	isotropic	dilute liquid
1300	0.504	isotropic	liquid
1498	0.581	isotropic	dense liquid
1775	0.689	~	liquid-hexatic coexistence
1785	0.693	~	liquid-hexatic coexistence
2142	0.831	sixfold modulation; square-root Lorentzian line shape	hexatic
2180	0.846	~	hexatic-solid coexistence
2208	0.857	~	hexatic-solid coexistence
2247	0.874	sixfold modulation; Lorentzian line shape	solid
2376	0.926	sixfold modulation; Lorentzian line shape	solid

thermodynamic limit for this phase. Nevertheless, finite-size effects modify the observed form so that the sixfold modulations expected from a long-range ordered solid may still be observed in the quasi-long-range ordered hexatic. The power-law exponent η_6, given by Eq. (3.4), is related to the Frank constant K_A,

$$\eta_6 = \frac{18 k_B T}{\pi K_A}. \tag{3.6}$$

The Frank constant depends on the distortions in the bond angle field; its magnitude reflects the mechanical stability (manifested as bond orientational order) of the hexatic phase, much as the elastic constant K determines the limit of mechanical stability of the solid. The quasi-long-range bond orientational order of the hexatic phase is destroyed by free disclinations generated by a disclination unbinding. Only a very small concentration of disclinations is necessary to reduce the system to an isotropic fluid state. The KTHNY theory predicts that the disclination unbinding transition is also continuous, and that it occurs when the value of the Frank constant falls below $(72/\pi)k_BT$. Near the disclination unbinding transition, η_6 is expected to approach the value of 0.25.

The KTHNY theory does not preclude the possibility that the solid may become thermodynamically unstable with respect to the isotropic fluid phase at a point where it is still mechanically stable with respect to dislocation pair unbinding (i.e., $K > 16\pi$). In this case the core energy E_c associated with the formation of a free dislocation must be less than the cutoff $2.84 k_B T$, so that a spontaneous proliferation of grain boundaries is the primary mechanism for reaching the limit of mechanical stability (which is taken to be the melting point) [6,29]. For this reason, the free dislocation core energy is an important predictor of the melting mechanism.

Chou and Nelson generalized the KTHNY theory to show how defect-mediated melting can be incorporated into the schematic phase diagram for particles with short-ranged interactions. Following the lead given by the simulations of Bladon and Frenkel, they analyzed the properties of a two-dimensional model system in which there is coupling between a first order isostructural solid-solid transition and the elastic deformations that these phases can support. The key notion is that, because the compressibility diverges at the isostructural transition critical point, near that critical point the bulk modulus must decrease, and thereby permit an increase in the concentration of free dislocations. In turn, the increased concentration of free dislocations can induce the formation of a hexatic phase. They show that the critical exponents of the ordered solid-to-hexatic phase transition are the same as inferred from the standard KTHNY theory.

Table I lists the different sample densities used in our investigations and the thermodynamic states we have assigned to them. Figure 4 displays sample configurations at six of these densities: $\rho^* = 0.58$, 0.69, 0.83, 0.86, 0.88, and 0.93. Proceeding from the lowest to the highest density, these figures show the system in (A) the pure liquid state, (B) a state with coexistence between liquid and hexatic phases, (C) the pure hexatic phase, (D) a state with coexistence between hexatic and solid phases, (E) the solid close to the hexatic-solid transition, and (F) a compressed solid.

The identities of the pure phases were established by computing the static correlation functions from statistical averages of the particle positions. For example, the static structure function was computed from

$$S(\mathbf{Q}) = N^{-1} \sum_i \sum_j \langle \exp[i\mathbf{Q}\cdot(\mathbf{R}_i - \mathbf{R}_j)] \rangle. \tag{3.7}$$

In Fig. 5 we show the two-dimensional structure functions corresponding to the same (A) fluid, (B) hexatic, and (C) solid phase densities described in Fig. 4. Also shown are sample Voronoi constructions (D–F) where the patterns of defects have been included in the color scheme. The concentration of bound dislocation pairs in the pure solid phase close to the solid-hexatic phase transition is small ($<0.1\%$)

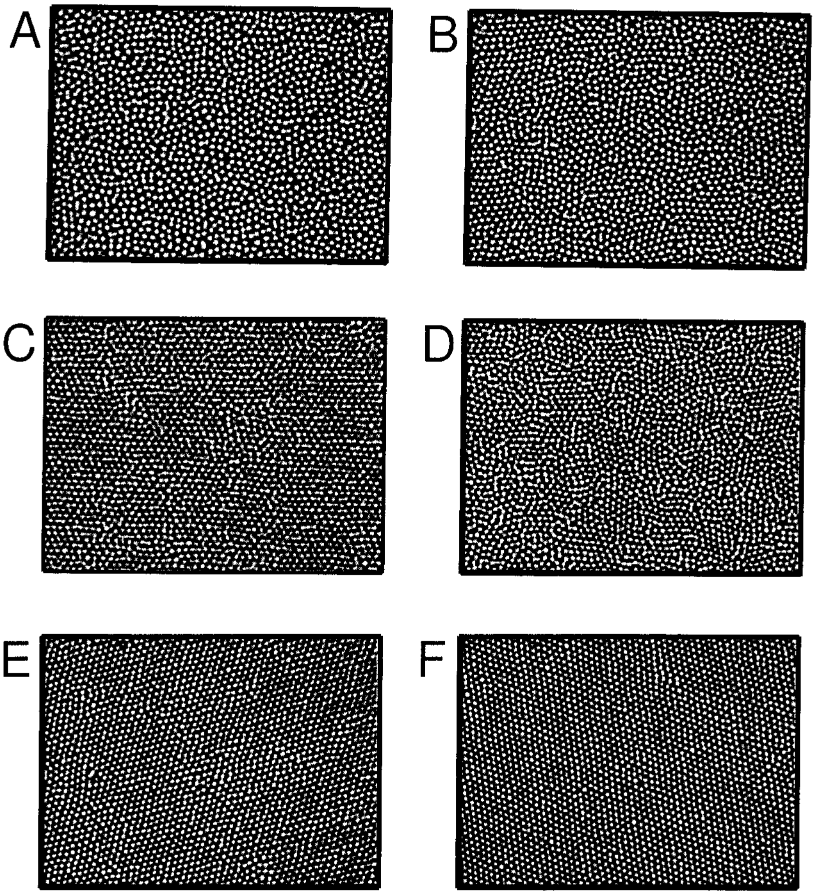

FIG. 4. Sample particle configurations of the quasi-two-dimensional assembly of PMMA spheres with frame size 224×41 μm^2 and $N \sim 2000$ particles (see Table I). Each frame represents an equilibrium state of the system: (A) the pure liquid state, $\rho^* = 0.58$; (B) a state with coexistence between liquid and hexatic phases, $\rho^* = 0.69$; (C) the pure hexatic phase, $\rho^* = 0.83$; (D) a state with coexistence between hexatic and solid, $\rho^* = 0.86$; (E) the solid close to melting, $\rho^* = 0.88$; and (F) a compressed solid, $\rho^* = 0.93$.

so that the dislocation core energy must be larger than the $2.84 k_B T$ cutoff predicted by Chui [6]. We thus conclude that this system falls within the regime where the KTHNY theory should be valid. We return to a more careful consideration of the defect core energies in Sec. IV.

The sixfold angular symmetry exhibited in Fig. 5B is a necessary but not sufficient condition to distinguish this phase as hexatic. Our identification is further supported by the very good fit, shown in Fig. 6B, of the transverse angular dependent line shape of the structure function to a square-root Lorentzian (SRL), $S(\theta_0) = \{[\theta_0 - \chi]^2 + \kappa^2\}^{-1/2}$ where θ_0 is the angular position of the first peak in the static structure function, χ is the in-plane angle that ranges from zero to 2π, and κ is the SRL angular width. The SRL functional form of the line shape has been established as a signature of hexatic order [30]. Also shown in Fig. 6 are the line shapes of (curve A) the isotropic fluid and (curve B) the dense solid phase (which is well fit by a simple Lorentzian function).

In Fig. 7 are shown the results of our analyses of the respective pair correlation functions; these results provide conclusive evidence for the assignments we have made of the character of the pure phases mentioned above. The translational correlation functions were obtained by computing histograms of the measured distribution of particle separations from

$$g(r) = \rho^{-2} \left\langle \sum_i \sum_{j \neq i} \delta(\mathbf{r}_i)\, \delta(\mathbf{r}_j - \mathbf{r}) \right\rangle. \tag{3.8}$$

In an analogous fashion, the global bond orientational correlation functions were computed from Eqs. (3.4) and (3.5).

The positional order in the solid phase is seen to decay with increasing particle separation as $\sim r^{-1/3}$ [see the dotted curve labeled A for $g(r)$ in Fig. 7], while the angular order does not decay at all. Thus, both the translational and bond orientational correlation functions for the solid phase behave consistently within the KTHNY framework. The observed value of the power law exponent, $\eta = \frac{1}{3}$, suggests that (within the context of the KTHNY theory) the solid is very close to the dislocation unbinding transition. It will be shown in Sec. V, however, that this density is in fact close to a first order solid-to-hexatic transition.

In the hexatic phase we find that the translational order decays exponentially with increasing particle separation as $\sim \exp[-r/(1.8\ \mu\text{m})]$, while the angular order decays as these observations are also in agreement with the predictions of KTHNY theory. The observed value for the bond orientational power law exponent, $\eta_6 = \frac{1}{4}$, suggests that (again, within the context of the KTHNY theory) the system is very close to a continuous disclination unbinding transition. In this case, however, we find that this density is far from a transition to the isotropic fluid and that the hexatic-to-liquid transition is also strongly first order. In the fluid phase, both the positional order and the angular order decay exponentially with increasing particle separation.

IV. DEFECT ANALYSIS

As mentioned in Secs. II and III, a necessary condition for the KTHNY theory to apply to the melting of any experimental quasi-two-dimensional system is that the ‘‘core’’ energy associated with the unbinding of dislocations is larger

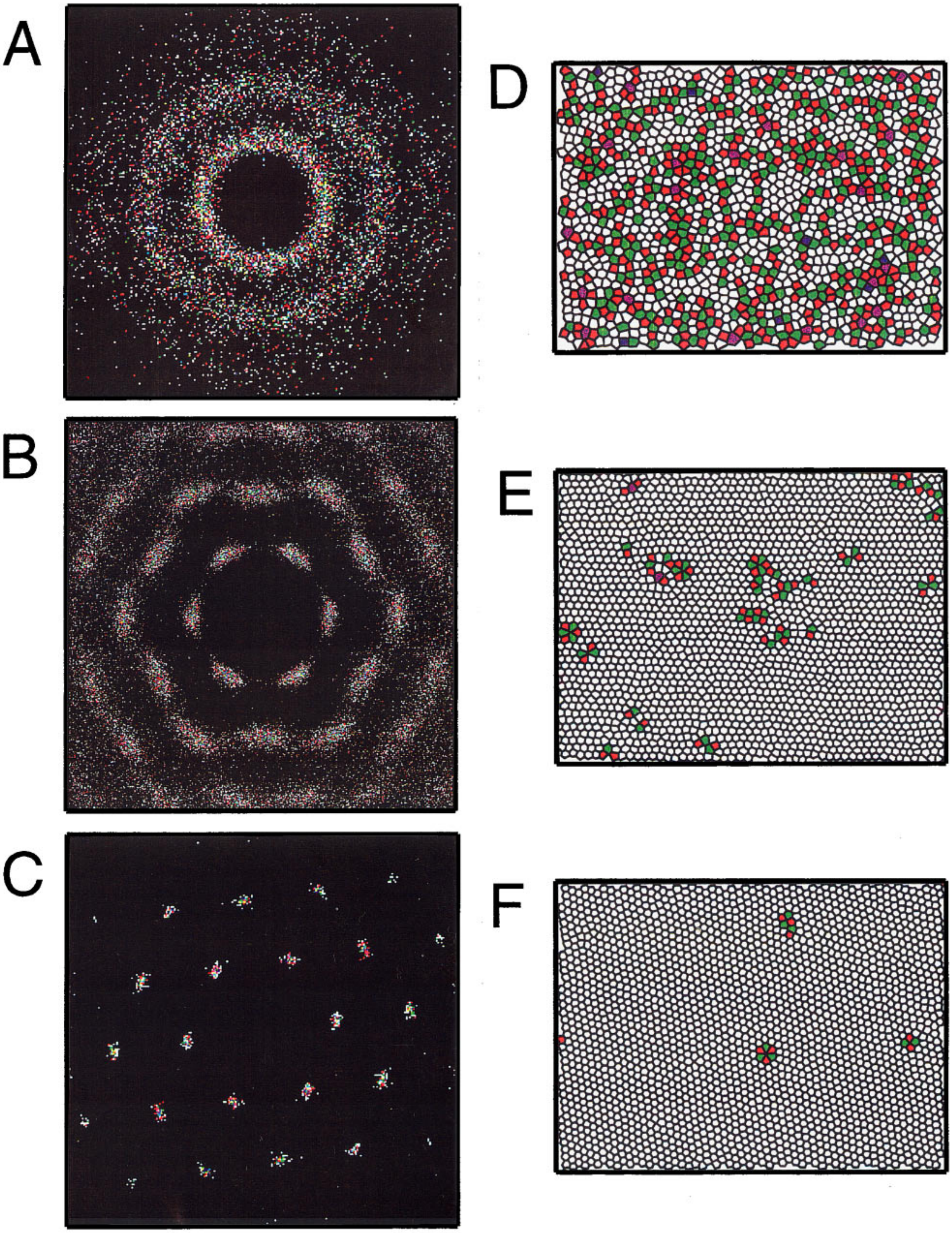

FIG. 5. Computed two-dimensional structure functions corresponding to (A) the pure liquid state, $\rho^*=0.58$; (B) the pure hexatic phase, $\rho^*=0.83$; and (C) a compressed solid, $\rho^*=0.93$. Also shown are the Voronoi constructions of sample configurations at the same densities: (D) $\rho^*=0.58$, (E) $\rho^*=0.83$, and (F) $\rho^*=0.93$. The color coding is the same as that described for Fig. 3. In panel (F), a vacant particle appears as a circular bound group of three dislocations.

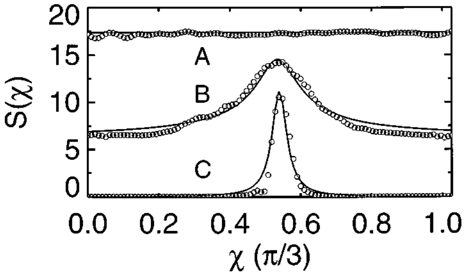

FIG. 6. Angular dependences of the line shapes of the two-dimensional structure functions (evaluated at the wave vector corresponding to the first peak, $|\mathbf{k}_{\max}|$) shown in Figs. 5A–5C. The curves are displaced on the vertical scale for clarity. Curve A: $k_{\max}=5.2\ \mu\mathrm{m}^{-1}$. There is no angular dependence for the isotropic fluid phase, while the hexatic line shape (curve B) $k_{\max}=6.2\ \mu\mathrm{m}^{-1}$ agrees very well with a square-root Lorentzian (solid line, $0.48\times[(\chi-0.54\ \mathrm{rad})^2+(0.056\ \mathrm{rad})^2]^{-1/2}$; see text). The solid phase (curve C) $k_{\max}=6.4\ \mu\mathrm{m}^{-1}$ is well fit to a simple Lorentzian function, $0.007[(\chi-0.54\ \mathrm{rad})^2+(0.025\ \mathrm{rad})^2]^{-1}$.

than Chui's [6] predicted cutoff of $2.84k_BT$. In this section we present a detailed self-consistent analysis of the defect topologies and energies as a function of particle density.

It is evident from examination of Fig. 3 that all visible defect species, namely, free dislocations, dislocation pairs, as well as other defect topologies, appear and disappear on the time scale of successive video frames. It is also important to note that their absolute locations are temporally uncorrelated. From these observations alone, it is possible to conclude that the essential activated reversible processes, which involve the formation and motion of these defects, occur on time scales shorter than the 30-ms sampling time interval.

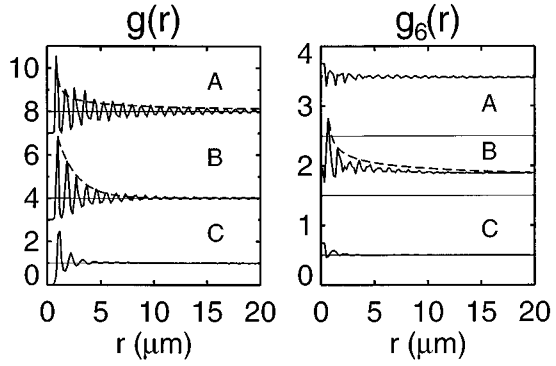

FIG. 7. Translational and bond orientational correlation functions as a function of particle density. The curves have been shifted vertically for clarity. For both sets of curves, the three pure phases are represented with the same densities as given in the previous figures. The envelope of $g(r)$ for the compressed solid (curve A) decays algebraically (dotted curve, $\sim r^{-1/3}$), while $g_6(r)$ remains constant. For the hexatic phase (curve B), $g(r)$ decays exponentially $\{\sim\exp[-r/(1.8\ \mu\mathrm{m})]\}$, while $g_6(r)$ decays algebraically ($\sim r^{-1/4}$). In the fluid state (curve C), both correlation functions decay exponentially.

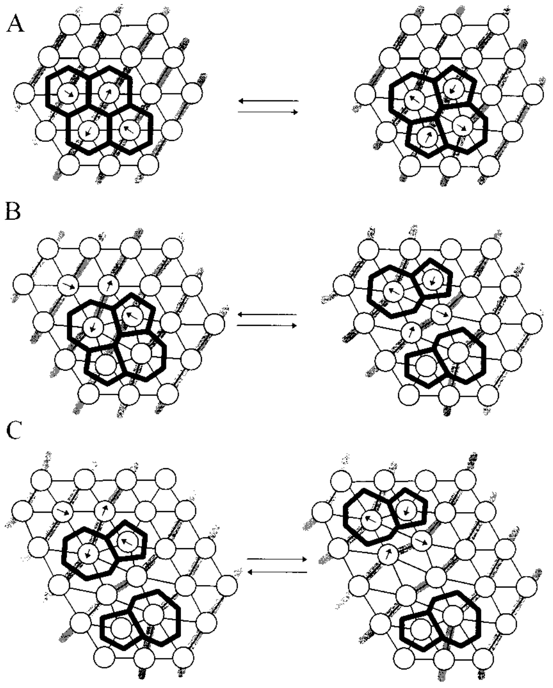

FIG. 8. Schematic depiction of dynamical reversible processes that involve defect formation and motion. (A) Paired dislocation formation or annihilation; (B) dislocation unbinding or binding; and (C) dislocation glide.

It is useful to consider in some detail the mechanisms corresponding to the interconversion of these defect species under equilibrium conditions. Figure 8 depicts three reversible processes: (A) the nucleation or annihilation of a bound dislocation pair; (B) the unbinding or binding of the same species, and (C) the translation of a free dislocation. The Voronoi polyhedra are superimposed in heavy black lines on top of the triangulated particle configurations. Each thermally activated process involves a change in configuration that results from the motion of as few particles as one, but may involve the concerted motion of several particles. Such particle motions are a consequence of thermal fluctuations in the system. In general, two particles that are not nearest neighbors can only form a new bond at the expense of breaking a bond already held between two other particles. The relative particle motions associated with the making and breaking of bonds are indicated with small arrows. Hence the nucleation of a dislocation pair (Fig. 8A) can be viewed as the simultaneous formation of two sevenfold- and two fivefold-coordinated sites from four original sixfold-coordinated sites. The resulting distortion in the bond angle field is localized to the region containing the paired dislocation. Another important feature is that the lattice vector registry (shown as heavy gray lines) is uninterrupted by the formation of a tightly bound dislocation pair. However, a similar fluctuation may give rise to dislocation unbinding (Fig. 8B) in which case the distortion of the bond angle field becomes delocalized and the lattice vector registry is interrupted due to the appearance of two inserted lattice row ends, each terminating at the fivefold-coordinated site of a free dislocation. Repetition of this process may lead to further separation of the free dislocations, and subsequently greater distortion of the bond angle field (Fig. 8C). The free energy for a pair of dislocations increases as the logarithm of their separation distance R and is given in elasticity theory by

$$\frac{F}{k_B T} = K\left[\ln\left(\frac{R}{a_c}\right) - \tfrac{1}{2}\cos^2(\phi)\right] + 2E_c, \tag{4.1}$$

where K is the elastic constant defined in Eq. (3.1), E_c is the ''core'' or internal energy associated with the formation of a free dislocation from the crystal, a_c is the ''core'' radius of a free dislocation, and ϕ is the angle between the vector joining the dislocations and the Burger's vector which depends on the orientations of the dislocations.

The mechanism discussed above for the motion of a free dislocation will only allow the defect to translate in a direction orthogonal to its axis (or Burger's vector). This type of motion is known as ''glide.'' Translation of a free dislocation in a direction parallel to its axis is called ''climb'' and, since this type of motion must implicitly involve many particle displacements, the glide mechanism is expected to be the dominant process of defect diffusion. An important consequence of the mechanisms described above is that free dislocations cannot spontaneously disappear, since this would involve the disappearance of an entire semi-infinite row end. A free dislocation can only be destroyed through binding with another free dislocation and subsequent annihilation.

Since the interconversion of defect species occurs under equilibrium conditions in our system, it is possible to determine the changes in free energy, enthalpy, and entropy associated with each of the processes illustrated in Fig. 8 by statistically sampling the particle configurations. We will make use of the fact that for any given defect transformation there is a conservation of topology. It is then possible to notate each process in general as an equilibrium expression:

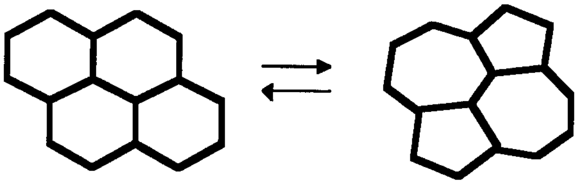

dislocation
formation or annihilation (4.2)

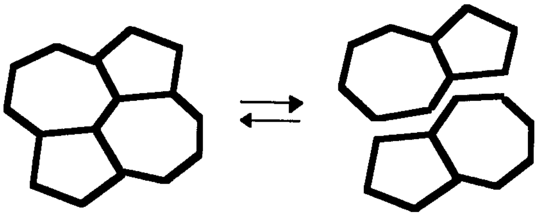

dislocation
unbinding or binding (4.3)

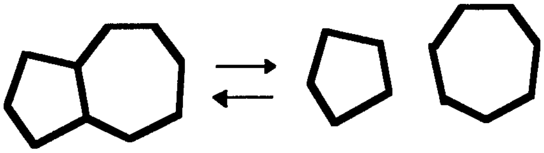

disclination
unbinding or binding (4.4)

Equations (4.2), (4.3), and (4.4) can be combined to obtain expressions for the direct formation of free dislocations or free disclinations from the undistorted crystal. The expression for free dislocation formation is given by adding the first two equations: Eq. (4.2)+Eq. (4.3). The expression for free disclination formation is given by [Eq. (4.2)+Eq. (4.3)] +2×[Eq. (4.4)].

The change in free energy is determined according to the formula

$$\Delta G = -k_B T \ln[K_{\mathrm{eq}}], \tag{4.5}$$

where K_{eq} is the equilibrium constant corresponding to the process under consideration. For the case of dislocation pair formation [Eq. (4.2)], K_{eq}=[paired dislocations]/[sixfold sites]^4; for dislocation unbinding [Eq. (4.3)], K_{eq}=[free dislocations]^2/[paired dislocations]; for disclination unbinding [Eq. (4.5)], K_{eq}=[fivefold sites][sevenfold sites]/[free dislocations]. The terms in the square brackets are concentrations expressed as number fractions. Equation (4.5) may be used to calculate the free energy from data such as that shown in Fig. 3, provided a good statistical sampling can be achieved.

We estimate the change in entropy using the expression

$$\Delta S = -k_B \ln\left[\frac{\langle A_f^{\mathrm{def}}\rangle}{\langle n A_f^{6-f}\rangle}\right] \tag{4.6}$$

where $\langle A_f^{\mathrm{def}}\rangle$ is the average free area available to the particles inside a given defect at a certain bulk density, and $\langle nA_f^{6-f}\rangle$ is the average free area available to the same number of

TABLE II. Defect statistics from particle trajectory data. $\langle n \rangle$ is the average number of defects per frame in a hundred frame sequence, $\langle A_f^{\mathrm{def}} \rangle$ is the average free defect area expressed in units of pix^2 [(0.17 μm)/pix] defined in the text, and is the defect number fraction. The total number of particles in the field of view is given in Table I.

	$\rho^*=0.83$			$\rho^*=0.88$			$\rho^*=0.93$		
Defect type	$\langle n \rangle$	$\langle A_f^{\mathrm{def}} \rangle$		$\langle n \rangle$	$\langle A_f^{\mathrm{def}} \rangle$		$\langle n \rangle$	$\langle A_f^{\mathrm{def}} \rangle$	
Free dislocations	5.8 ±2.2	22.0 ±1.6	0.003± 0.0010	3.3 ±0.4	23.0 ±2.4	0.002± 0.0006	1.4 ±0.8	18.5 ±2.3	0.0006± 0.0003
Dislocation pairs	15.1 ±3.4	43.5 ±2.9	0.007± 0.0016	9.9 ±2.4	44.6 ±2.8	0.004± 0.0011	1.1 ±0.8	45.4 ±5.8	0.0005± 0.0003
5-8-5 dislocations	4.5 ±2.0	39.6 ±5.9	0.002± 0.0009	0.95 ±0.9	38.8 ±6.0	0.0004± 0.0002	0.5 ±0.6	36.8 ±6.2	0.0002± 0.0002
fivefold disclinations	6.2 ±2.1	8.8 ±0.9	0.003± 0.0010	2.8 ±1.3	9.4 ±1.3	0.001± 0.0005	0.8 ±1.0	8.1 ±2.7	0.0003± 0.0001
sevenfold disclinations	5.0 ±1.4	13.6 ±1.9	0.003± 0.0012	2.2 ±0.6	11.9 ±1.8	0.0004± 0.0003	0.6 ±1.2	10.1 ±3.0	0.0003± 0.0001
site vacancies	1.9 ±0.8	~	0.001± 0.0012	0.4 ±0.6	~	0.0002± 0.0002	0.3 ±0.5	~	0.0001± 0.0003
nondefect sites	2,116	8.7	0.9892	2,274	9.1	0.9949	2,375	7.8	0.9991

particles confined to sixfold-coordinated sites at the same bulk density. The average free areas described in Eq. (4.6) were evaluated from the particle coordinates by numerically computing the areas of the Wigner-Seitz cells associated with individual defects or sixfold-coordinated sites and subtracting the cross-sectional area of the particles $(A_p = \pi\sigma^2/4)$.

Once the changes in free energy and entropy are known, the change in enthalpy can be calculated from the difference,

$$\Delta H = \Delta G + T\Delta S. \tag{4.7}$$

The change in enthalpy for a process that occurs at constant pressure is analogous to the change in internal energy for a constant volume process. Since our experimental system is held at constant pressure and chemical potential, the changes in enthalpies associated with defect transformations are the more relevant quantities.

Table II lists the different defect species considered in our analysis, the average number of observed occurrences per configuration during a 100-frame sequence, the average free area associated with a particular defect, $\langle A_f^{\mathrm{def}} \rangle$, and the number fractions. Also tabulated are the root mean square (rms) areas and rms number of occurrences. The analysis was carried out for three particle densities: $\rho^*=0.83$, 0.88, and 0.93, corresponding to the hexatic phase, the solid phase close to the melting transition, and a high-density solid phase. The sizes of the frames examined were such that, for each frame sequence, approximately 2000 particles were in the field of view. This information was used to calculate the equilibrium constants associated with Eqs. (4.2)–(4.4). Table III lists the changes in free energies, entropies, and enthalpies associated with each defect transformation. In general, the magnitudes of all three quantities increase with increasing particle density. It is also seen that dislocation unbinding [Eq. (4.3)] requires $\sim 2k_BT$ more energy (or enthalpy) than paired dislocation formation [Eq. (4.2)] while disclination unbinding requires only $\sim 1k_BT$ more in energy. The linear combinations corresponding to free dislocation formation and free disclination formation are also tabulated. From these values we obtain the ''core'' energies, entropies, and ethalpies associated with free dislocation and disclination formation. Interestingly, the magnitudes of the core quantities appear to be very similar for both dislocation and disclination formation at all three particle densities. Since the core enthalpy is far above the $2.84k_BT$ cutoff, we conclude that our system does meet the necessary criterion for the KTHNY theory to apply to the system we have studied.

V. COEXISTENCE AND FIRST ORDER TRANSITIONS

It was stated previously that we have observed strongly first order solid-to-hexatic and hexatic-to-solid phase transitions. This assertion is qualitatively supported by our observation that the dynamical behavior of our system is uniformly distributed at the particle densities we identified as pure phases (see Sec. III) while there are distinct dynamical heterogeneities at the densities we now identify as coexistence regions. In Fig. 9 are plotted trajectory maps of particle displacements corresponding to the particle densities shown in Fig. 4. Each map consists of 20 sequentially linked particle positions so that the full time duration is 600 ms. Although the behavior seen in Figs. 9B and 9D is suggestive of two-phase coexistence, bimodal distributions (e.g., in the velocity autocorrelation function) by themselves do not necessarily imply this situation. It is instead necessary to demonstrate statistical correlations between local quantities such as dynamical variables and stationary order parameters; such joint particle distributions may be used to distinguish between different coexisting phases at a single bulk density.

Our conclusions are based on an analysis of two local static variables and one local dynamical variable. These are

TABLE III. Defect-free energies, entropies and enthalpies of formation. Energies and enthalpies are expressed in units of k_BT. Entropies are in units of k_B.

	$\rho^*=0.83$			$\rho^*=0.88$			$\rho^*=0.93$		
Transformation	ΔG	ΔS	ΔH	ΔG	ΔS	ΔH	ΔG	ΔS	ΔH
Eq. (4.2) paired dislocation formation	4.90 ±0.2	0.22	5.12 ±0.2	5.43 ±0.2	0.20	5.63 ±0.2	7.60 ±0.2	0.38	7.98 ±0.2
Eq. (4.3) free dislocation unbinding	6.88 ±0.2	0.46	7.34 ±0.2	7.55 ±0.2	0.46	8.01 ±0.2	7.24 ±0.5	0.35	7.59 ±0.5
Eq. (4.2)+Eq. (4.3) free dislocation formation	11.79 ±0.3	0.68	12.46 ±0.3	12.98 ±0.4	0.66	13.64 ±0.4	14.84 ±0.5	0.73	15.57 ±0.5
‘‘core’’ quantities per free dislocation	5.90	0.34	6.23	6.49	0.33	6.82	7.42	0.36	7.78
Eq. (4.4) free disclination unbinding	5.77 ±0.2	0.44	6.21 ±0.2	6.79 ±0.2	0.28	7.07 ±0.2	8.80 ±0.7	−0.12	8.68 ±0.7
[Eq. (4.2)+Eq. (4.3)] +2×Eq. (4.4) free disclination formation	23.33 ±0.2	1.56	24.89 ±0.2	26.56 ±0.4	1.22	27.78 ±0.4	32.44 ±0.9	0.49	32.93 ±0.9
‘‘core’’ quantities per free disclination	5.83	0.39	6.22	6.64	0.30	6.94	8.11	0.12	8.23

the local bond orientational order parameter, $\psi_6(r_i)$, defined by Eq. (3.5), the local areal density, which we define as

$$\rho(r_i)=\frac{1}{A_i}, \tag{5.1}$$

and the local characteristic time required for a particle to diffuse a distance equal to its diameter,

$$\tau(r_i)=\frac{\sigma^2}{D_s(r_i)}, \tag{5.2}$$

with

$$D_s(r_i)=\lim_{t\to\infty}\frac{1}{4}\frac{d\langle[\mathbf{r}_i(t)-\mathbf{r}_i(0)]^2\rangle}{dt}. \tag{5.3}$$

In Eq. (5.1), A_i is the area of the Voronoi polyhedron assigned to particle i. The Voronoi polyhedron is a generalization of the Wigner-Seitz cell which is the simplest possible unit cell for a two-dimensional system. In Eq. (5.3), $D_s(r_i)$ is the asymptotic temporal limit of a locally defined self-diffusion coefficient. We have previously shown [31] that, for our system, $D_s(r_i)$ reaches its asymptotic value within 20 experimental sampling time intervals (600 ms).

The stationary order parameters, $\psi_6(r_i)$ and $\rho(r_i)$, both have magnitudes that are largest in the ordered solid phase; their values are considerably smaller at liquid densities. If the system exists as a pure phase, fluctuations in both order parameters are expected to occur randomly and to be uncorrelated with one another. On the other hand, if two phases coexist at the same bulk density the constituent particles of the two phases will separately contribute to different peaks in the joint probability distribution $P(\psi_6(r_i),\rho(r_i))$. That is, the fluctuations in the two order parameters will appear to be correlated.

Unfortunately, because our observation window contains a finite number of particles ($N\sim2000$), fluctuations of the order parameter values (which go as $N^{-1/2}$) will cause significant overlap between closely spaced peaks that appear in the distributions of $\psi_6(r_i)$ and $\rho(r_i)$. For this reason we consider slightly different local correlation functions, each defined as the absolute value of the projection of the order parameter onto a local average of the same function over nearest neighbors, namely,

$$m_{\psi_6}(r_i)=\left[|\psi_6(r_i)|\frac{1}{n}\sum_j|\psi_6(r_j)|\right]^{1/2} \tag{5.4}$$

and

$$m_\rho(r_i)=\left[\rho(r_i)\frac{1}{n}\sum_j\rho(r_j)\right]^{1/2}, \tag{5.5}$$

where the index j counts the ith particles n nearest neighbors. The values of the nearest-neighbor correlation functions defined by Eqs. (5.4) and (5.5) are expected to be more sensitive to the environments of particles which are not close to a phase boundary than the local order parameters themselves, because the local correlation functions are maximized for particles that are both well ordered (or dense) and have nearest neighbors that are also well ordered (or dense). In a similar spirit to that used in the definitions given by Eqs. (5.4) and (5.5), we also define a nearest-neighbor correlation function for the characteristic time

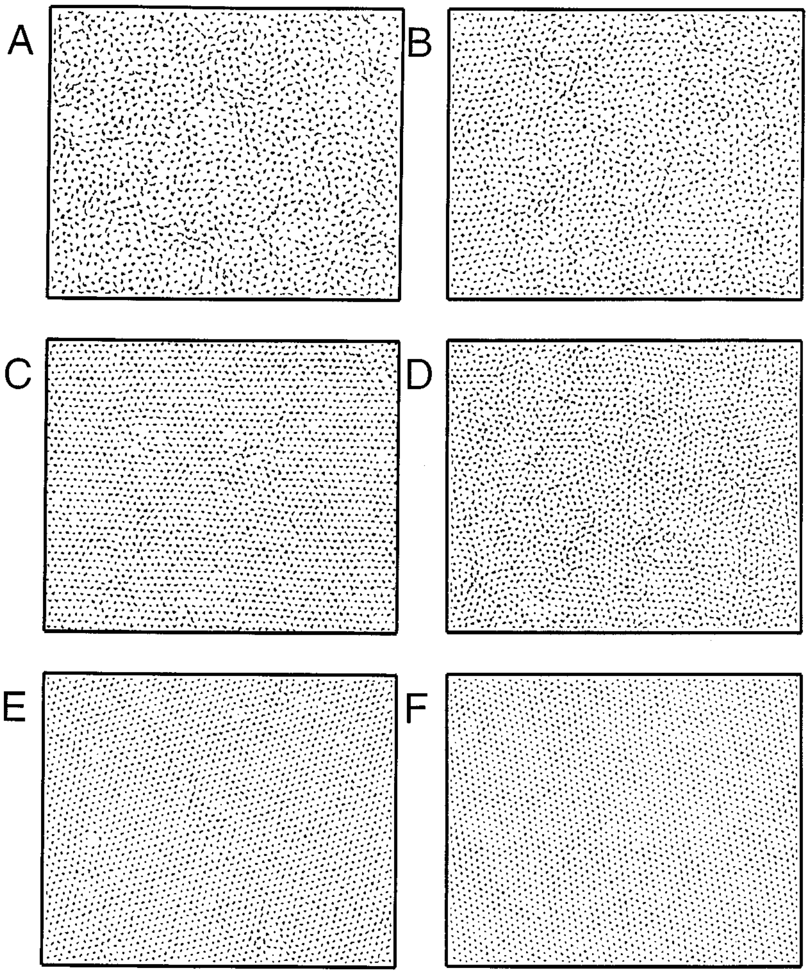

FIG. 9. Particle trajectories as a function of density. Line segments connect the particle positions between successive video frames. The durations of these sequences are for 20 frames or 660 ms. The densities are the same as those given in Fig. 4. The self-displacements of the ensemble of particles are seen to be uniform for the cases of the pure phases (frames A, C, E, and F), while they are inhomogeneous for the densities that represent coexistence (frames B and D).

$$m_{\tau_i} = \left[\tau_i \frac{1}{n} \sum_j \tau_j \right]^{1/2}. \tag{5.6}$$

It has been shown by Larsen and Grier [32] that the joint distribution $P(|\psi_6|, m_{\psi_6})$ is clearly bimodal in systems that exhibit solid-liquid coexistence. They classify a particle located at position i as belonging to the solid phase if the condition $m_{\psi_6}(r_i) + |\psi_6(r_i)| > C$ is satisfied, where C is an empirically determined constant that bounds the two distributions in the m_{ψ_6}-$|\psi_6|$ plane. If the above-stated condition is not satisfied, the particle located at position i is assigned to the fluid phase.

For the data sets with particle densities in the range $\rho^* = 0.58–0.93$, we have calculated the joint distributions $P(\rho, m_\rho)$, $P(|\psi_6|, m_{\psi_6})$, and $P(\tau, m_\tau)$. In Fig. 10 are shown two-dimensional scatter plots of these distributions taken from a single-particle configuration at two particle densities we identified as lying in the fluid and hexatic regions of the phase diagram ($\rho^* = 0.58$ and 0.83, respectively). For both densities, it can be seen that all three curves are well represented as single distributions. A similar behavior was observed for the distributions at densities characteristic of the pure solid phase. Clearly, these distributions are very different from the bimodal distributions seen at bulk densities corresponding to coexistence regions. For example, in Fig. 11 we show joint distributions for particle densities $\rho^* = 0.69$ and 0.85 which lie, respectively, within the fluid-hexatic and hexatic-solid coexistence regions. The dotted lines indicate the values of the cutoff C we have chosen to distinguish between the two peaks. Note that the peak widths and positions corresponding to the hexatic components are, within statistical error, the same as that for the distributions characteristic of the pure hexatic phase, shown in Fig. 10.

To demonstrate that the bimodal fluctuations are correlated between the different order parameters, we identify the particles that contribute to the separate peaks in the bimodal distributions. Figure 12 shows a comparison of the particle assignments we have made according to the analysis described above using Voronoi constructions of the particle configurations. Figures 12A, 12B, and 12C correspond to a particle density that lies in the pure fluid region of the phase diagram ($\rho^* = 0.58$), while Figs. 12C, 12D, and 12E ($\rho^* = 0.83$) correspond to the hexatic phase region. Similarly, Figs. 13A, 13B, and 13C display results of the analysis for the fluid-hexatic coexistence region ($\rho^* = 0.69$), while Figs. 13C, 13D, and 13E ($\rho^* = 0.85$) correspond to the hexatic-solid coexistence region. The gray scale shading indicates the partitioning of the particles between pure phases; the fluid phase is labeled white, the hexatic phase is labeled light gray, and the solid phase is labeled dark gray. In Figs. 12, 13A, and 13D, the assignment of particles to phases was made according to an analysis of the local densities [i.e., $P(\rho, m_\rho)$], while in Figs. 12, 13B, and 13E, the assignment

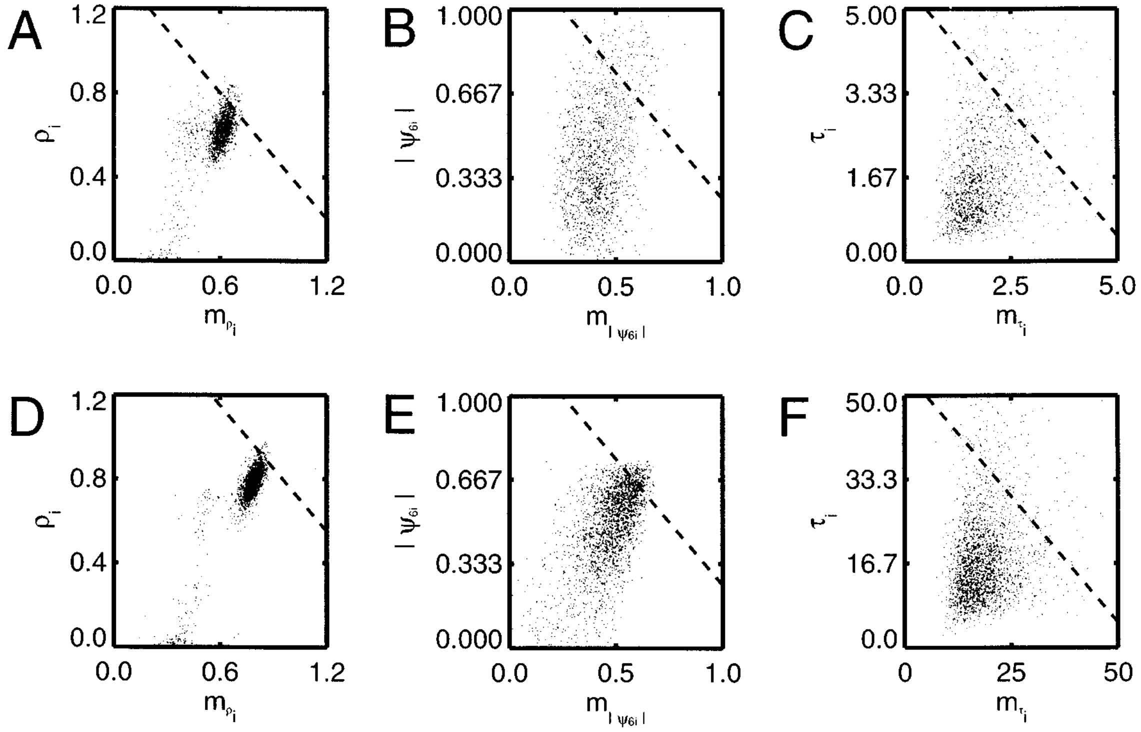

FIG. 10. Two-dimensional scatter plots of the three local order parameters used in our analysis, $\rho(r_i)$, $\psi_6(r_i)$, and $\tau(r_i)$, vs their nearest-neighbor averages m_{ρ_i}, $m_{\psi_{6i}}$, and m_{τ_i} for the pure liquid ($\rho^*=0.58$, plots A, B, and C) and hexatic ($\rho^*=0.83$, plots D, E, and F) phases. In all cases, the density of points is well described as a single distribution. The dashed lines indicate the value of the constant C used to distinguish between possible coexisting phases in the systems. They are (A) 1.4, (B) 1.4, (C) 5.2, (D) 1.8, (E) 1.4, and (F) 65.

was entirely based on an analysis of the local bond orientational order parameters $[P(|\psi_6|,m_{\psi_6})]$; in Figs. 12, 13C, and 13F, the assignments are based on an analysis of the local correlation times $[P(\tau,m_\tau)]$. For both pure phases shown in Fig. 12, the three order parameter analyses are unique, while for the coexistence bulk densities (Fig. 13), the three analyses give nearly the same results. Thus, at the coexistence densities, the partitioning of the distributions in the three order parameters do not occur randomly with respect to one another. We therefore conclude that two phases, each with their own distinct average properties, coexist under equilibrium conditions at these particle densities.

We illustrate the cumulative results of our analysis by computing the intersection of all three joint distributions: $P(|\psi_6|,m_{\psi_6})\cap P(\rho,m_\rho)\cap P(\tau,m_\tau)$. In Fig. 14 are shown Voronoi constructions of the particle configurations displayed in Fig. 4. The color scheme indicates the assignment of particles to phases as described in Figs. 12 and 13, although the assignments are now made according to the intersection described above.

Our conclusion that the particle densities examined in Fig. 13 are examples of coexisting phases, hence of first order transitions between the coexisting phases, is further supported by the consistency of our results with the lever rule [33]. The relative amounts of the two phases in the coexistence region of a first order transition are expected to satisfy the simple relation

$$\frac{n_\alpha}{n_\beta}=\frac{l_\beta}{l_\alpha}. \tag{5.7}$$

In Eq. (5.7), n_α is the number of particles assigned to phase α, n_β is the number of particles assigned to phase β, $l_\alpha=|\rho^*-\rho^*_\alpha|$, and $l_\beta=|\rho^*-\rho^*_\beta|$. The transition densities ρ^*_α and ρ^*_β are found by examining separately the previously determined binary components of the local density distributions. In Fig. 15 we show histograms of the local order parameter, $\rho(r_i)$, at particle densities $\rho^*=0.689$ (Fig. 15A) and 0.846 (Fig. 15B). Each figure displays the total density distribution and the binary component distributions. The solid curves associated with the component data sets are linear least square fits of Gaussian functions to the distributions, while the solid curves passing through the total density distributions are the sums of the component Gaussian fits. The peak positions (indicated with dashed lines) indicate the transition densities, while the area under each Gaussian function is proportional to the amount of the respective phase. In Figs. 15C and 15D we show the results of a similar analysis using the bond orientational order parameter. See Table IV for the values of all parameters.

Table IV displays the peak positions and widths determined from our analysis as a function of particle density. The values corresponding to the component peaks of the distributions exhibiting coexistence are also given. In Table V the ratios l_α/l_β and n_β/n_α, estimated from the analysis, are shown. The quantities n_α and n_β are determined by evaluation of the integrated areas A_1 and A_2 of the Gaussian fits to the binary component peaks. The coexisting liquid and hexatic phase densities were determined to be 0.68 and 0.70, respectively, while the corresponding coexisting hexatic and solid phase densities are 0.83 and 0.87, respectively. At the

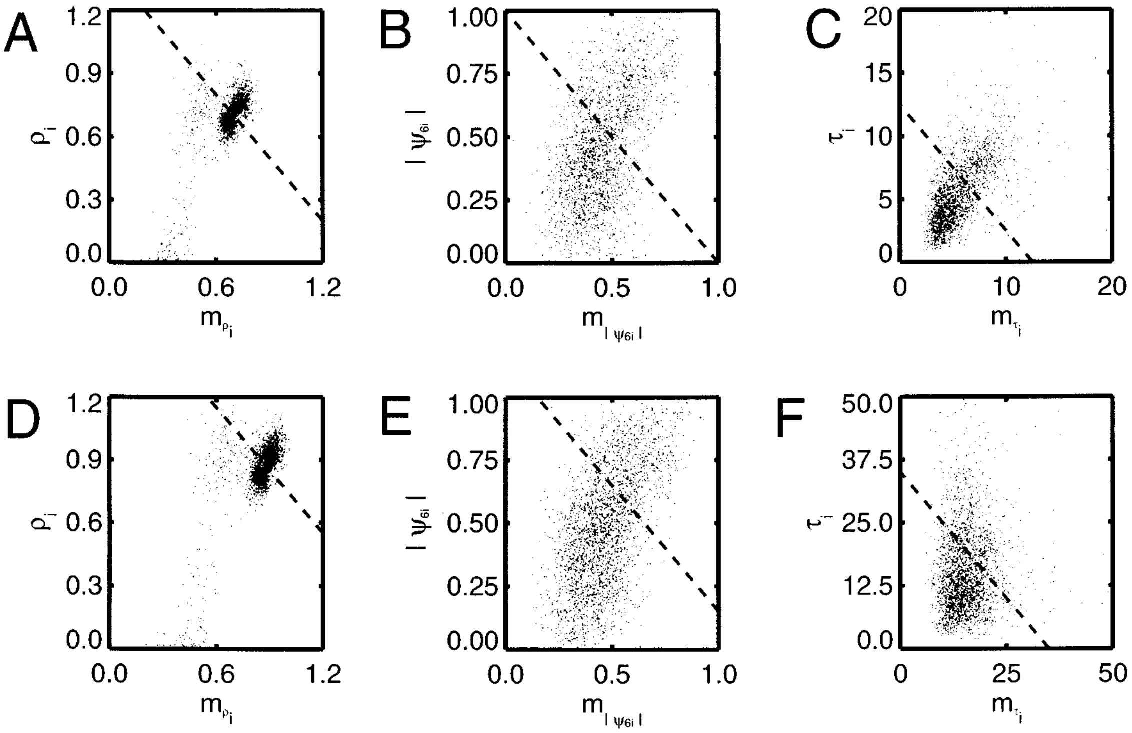

FIG. 11. Two-dimensional scatter plots similar to those shown in Fig. 10, evaluated at the densities corresponding to liquid-hexatic ($\rho^*=0.69$, plots A, B, and C) and hexatic-solid ($\rho^*=0.86$, plots D, E, and F) coexistence. In all cases, the data are well represented as bimodal distributions. The dashed lines indicate the value of the constant C used to distinguish between possible coexisting phases in the systems. They are (A) 1.4, (B) 1.0, (C) 12, (D) 1.8, (E) 1.2, and (F) 35.

same particle densities, the coexisting values of the bond orientational order parameter are 0.28 and 0.61 for the liquid and hexatic phases, respectively, and 0.63 and 0.75 for the hexatic and solid phases, respectively. The analogous coexistence values of the characteristic times are 4.27 and 4.48 s for the fluid-hexatic region, and 11.42 and 11.62 for the hexatic-solid region. When the cited values of the transition densities are substituted into Eq. (5.7), the lever rule is found to hold with a best accuracy of 1.7% and a worst accuracy of 14%.

VI. DISCUSSION

The experiments described in the preceding sections of this paper establish the existence of first order solid-to-hexatic and hexatic-to-liquid phase transitions in a pseudo-two-dimensional system of sterically stabilized PMMA colloidal particles. Bladon and Frenkel have shown, from Monte Carlo simulations, that the behavior we observed is to be expected for particles which have an interaction potential which supports an isostructural solid-to-solid phase transition. Our findings are also in agreement with the results of the analytical studies of Chou and Nelson [8], who examined the consequences of modifying the conventional KTHNY theory of two-dimensional melting to include coupling between an isostructural solid-to-solid phase transition and the strain fields in those solid phases. Because of the difficulties associated with establishing equilibrium in two-dimensional systems, and the difficulties associated with establishing the nature of the thermodynamic limit from examination of finite samples, we now examine some issues associated with the interpretation of our experimental data.

A key element in our analysis is the identification of densities for which there is two-phase coexistence. Assignment of a local region of the system to a particular phase depends on the definition of a suitable descriptor for that phase. If that descriptor, say the local density, has a bimodal distribution, it is plausible that the system examined does exhibit phase coexistence. However, the existence of a bimodal distribution of the local density in a finite sample is not, by itself, conclusive evidence of two-phase coexistence. In principle, to establish that a bimodal distribution of any single descriptor of phase identity is definitive evidence of two-phase coexistence it is necessary to show that the bimodal distribution persists in the thermodynamic limit, i.e., to study, at constant density, the system size dependence of the distribution. The evidence for the existence of two-phase coexistence at a particular density in a finite sample can be strengthened by the use of multiple descriptors and a coincidence analysis. Our identifications of the densities at which there is coexistence between the solid and hexatic phases and between the hexatic and liquid phases have utilized a triple coincidence analysis. We have shown that for a particular overall sample density, the local density, the local bond orientational order parameter, and the local diffusion coefficient are related by one-to-one maps; that is, they simultaneously locate the same regions in the images of the two-dimensional colloid system. We have identified those regions with the relevant phases. In contrast, the same triple coincidence analysis shows that there is no correlation between these descriptors in the pure

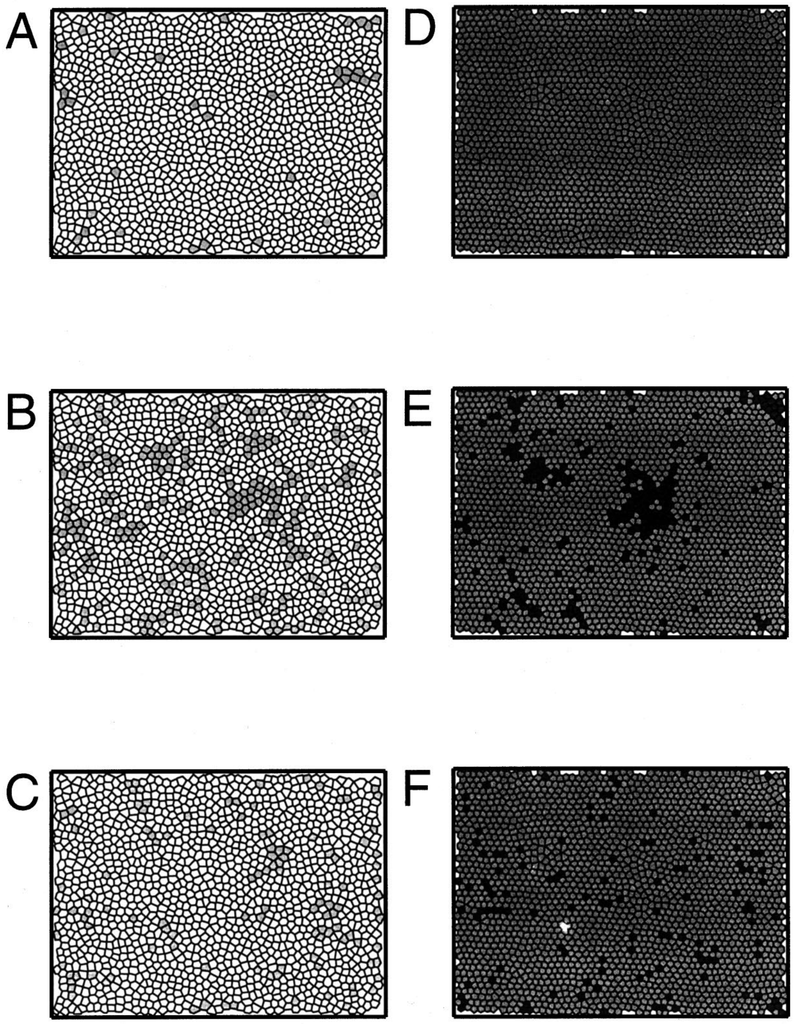

FIG. 12. Voronoi constructions of particle configurations corresponding to the liquid ($\rho^*=0.58$, plots A, B, and C) and hexatic ($\rho^*=0.83$, plots D, E, and F) phases. The gray scale scheme indicates the partitioning of the particles between phases; the fluid phase is labeled white, the hexatic phase is labeled light gray, and solid phase is labeled dark gray. Plots A and D correspond to the analysis of the joint distributions in local density, plots B and E correspond to the analysis of the local bond orientational order parameter, and plots C and F correspond to the analysis of the local correlation times.

liquid phase. We believe that the results of the triple coincidence analysis provide very strong support for the inferences we have drawn concerning the occurrence of first order phase transitions in the system studied.

As to the influence of finite sample size on the observed behavior, we have shown, in Sec. II, that the translational and bond orientation correlation functions are independent of subdivision of the video image of the sample system into subblocks, and that the correlation length for translational order is small compared to the size of the sample video image.

We have noted that on the time scale of successive video images of our system dislocations appear and disappear, and thus we inferred that our system is at equilibrium. That conclusion is supported by the observation that the effective diffusion coefficient of a dislocation is very large, since the appearance and disappearance of dislocations at uncorrelated positions in successive video frames implies an effective displacement per frame separation of the order of the size of the video image. Therefore, during a typical 72-h run a dislocation can sample the entire area of a video image, and can move a very large distance relative to the typical size of a one-phase region when there is hexatic-phase–solid-phase coexistence. In the worst case, in which equilibrium must be established by particle displacements, we note that the diffusion coefficient of a colloid particle in, say, the hexatic phase, is large enough ($D\sim 0.33$ $\mu\mathrm{m}^2/\mathrm{s}$) that a particle can move a distance equal to 585 particle diameters in a typical 72-h run. This distance is also greater than the typical size of a one-phase region when there is hexatic-phase–solid-phase coexistence.

In our experiments, each cell has a unique density, hence the density dependence of the properties of the system is studied by assembling the data for a large number of cells. As stated in Sec. II, although the method we used to adjust the sample cell thickness does not achieve uniform separation of the cell walls over the entire cell, the portion which is thin enough to constrain the colloid particles to one plane occupies the larger fraction of the total area of the cell. In fact, in our system the fraction of the sample which is quasi-two-dimensional is large enough to be considered the reservoir for the part of the sample that is thicker. Put another way, it is the chemical potential of the quasi-two-dimensional portion of the colloid sample that determines the state of the remainder, and not the reverse. We conclude that it is appropriate to interpret our results in terms of equilibrium at constant density.

One class of pair potentials that supports an isostructural solid-to-solid transition consists of a strongly repulsive core and a very short-ranged attractive well (or repulsive step). Simulations of two- and three-dimensional systems with a pair interaction of this type show that the isostructural tran-

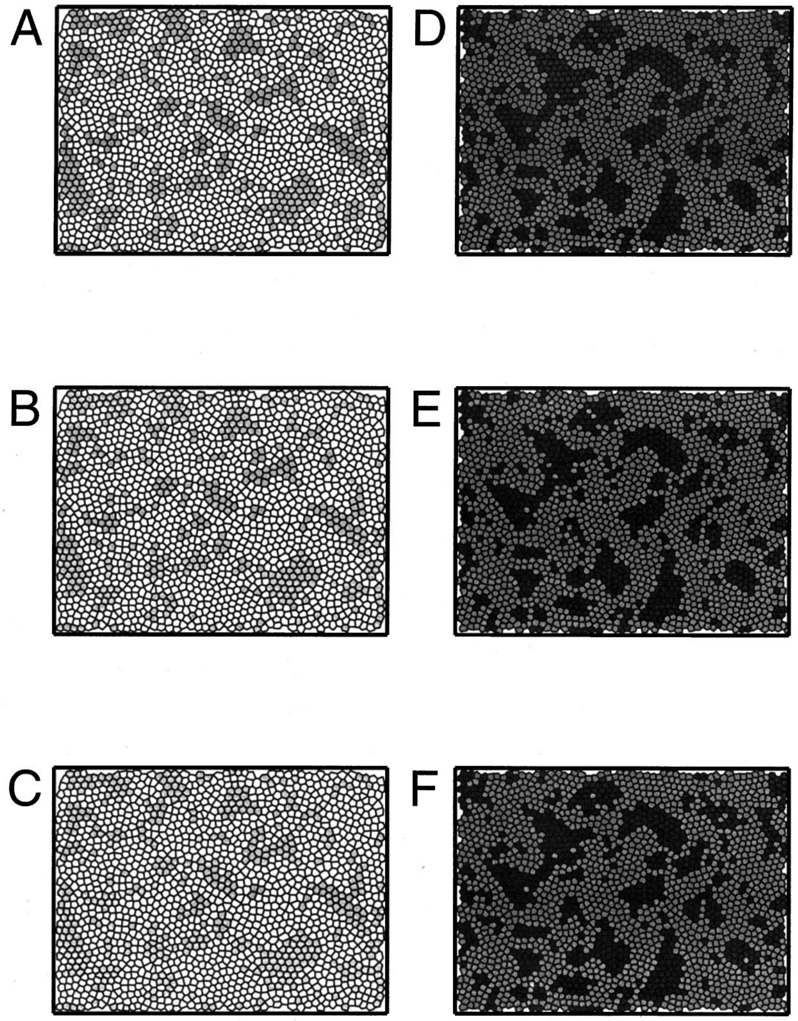

FIG. 13. Voronoi constructions of particle configurations corresponding to the liquid-hexatic ($\rho^*=0.69$, plots A, B, and C) and hexatic ($\rho^*=0.86$, plots D, E, and F) coexistence regions. As in Fig. 12, the gray scale scheme indicates the partitioning of the particles between phases. The plot ordering is the same as that shown in Fig. 12.

sition disappears from the phase diagram when the ratio of the width of the attractive well (or the repulsive step) to the repulsive core diameter exceeds a small critical value, which is about 0.08 for the two-dimensional hard disk plus square well interaction. We now examine the extent to which the effective interaction between the particles in the system we have studied satisfies the conditions under which one can reasonably expect the simulations of Bladon and Frenkel to be applicable.

The quasi-two-dimensional system we have studied consists of sterically stabilized PMMA spheres. The steric stabilization is achieved by grafting long chain molecules to the surface of each sphere; in our sample these chains create a brush with height about 300 Å. The effective interaction between a pair of sterically stabilized PMMA spheres then has a hard core with a diameter of about 1 μm and a softer interaction with a range of about 0.06 μm. The softer interaction, which is generated by the compression of the long chain brushes grafted to the surface of the PMMA particle, is repulsive over most or all of its range. If the long chains do not interpenetrate when the brushes begin to overlap, the interaction generated by the compression of the brush is positive everywhere because of the loss of chain configurational entropy which accompanies the brush compression. If the long chains do interpenetrate when the brushes begin to overlap, the interaction can be either repulsive or attractive. The former case is usually the only one considered; it always arises when there is no difference between the energies of chain element-chain element interaction and chain element-solvent interaction (the so-called athermal limit). The latter case can in principle occur over a small range of brush interpenetration near the onset of brush-brush contact, if the chain-element–chain-element interactions are more favorable than chain-element–solvent interactions.

Calculations of the interaction between interpenetrating brushes in the athermal limit have been reported by Martin and Wang [34]. They show that the segment density profile along the normal to the surface is sensibly unaffected by brush-brush interpenetration in the limit of very large chain length, and is increasingly affected as the chain length decreases. In particular, for chains of about the same length as used in the stabilization of our PMMA particles, overlap of the tails of the segment density profile creates a weak repulsion before the main parts of the brushes overlap; the repulsive force grows rapidly after the main parts of the brushes overlap. For our system the chain-element–chain-element interactions are expected to be more favorable than chain-element–solvent interactions, so we expect that the overlap of the tails of the segment density distribution will create a weak attraction before the main parts of the brushes overlap. Accepting this expectation, the effective particle-particle interaction in our system will have a weak and narrow attrac-

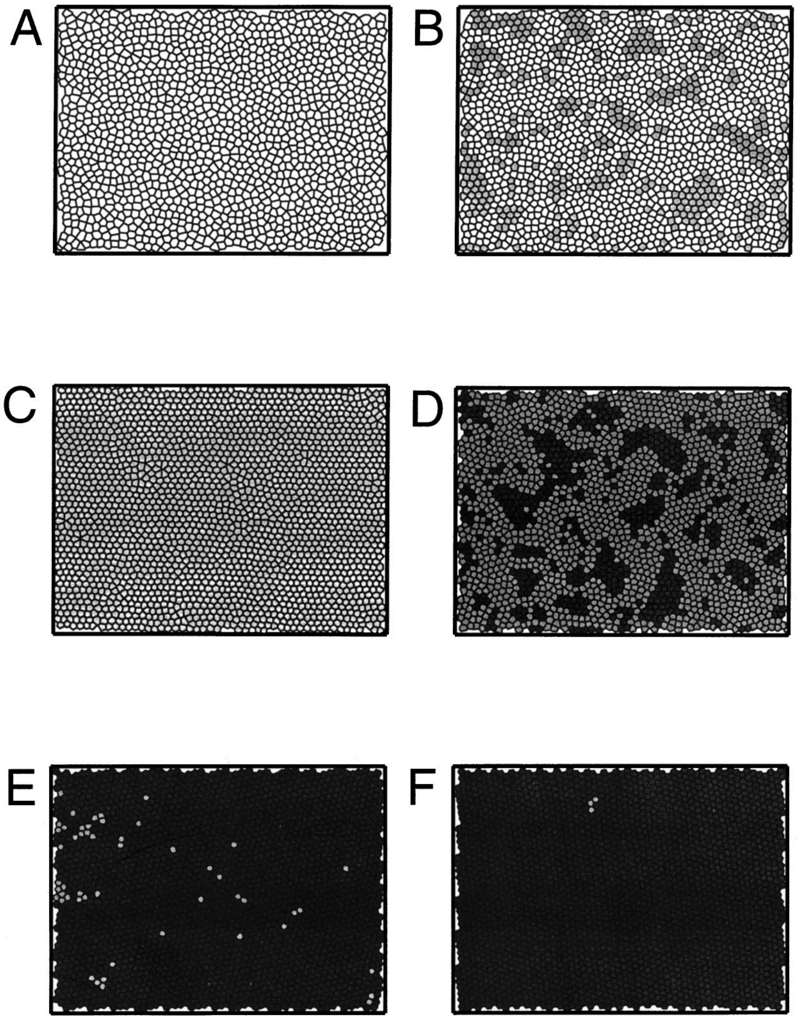

FIG. 14. Results of triple coincidence analysis using Voronoi constructions of particle configurations as a function of particle density. The gray scale scheme is determined by the intersection between the three joint probability distributions, $P(|\psi_6|,m_{\psi_6})$, $P(\rho,m_\rho)$, and $P(\tau,m_\tau)$. The densities corresponding to A–F are the same as in Figs. 4A–4F.

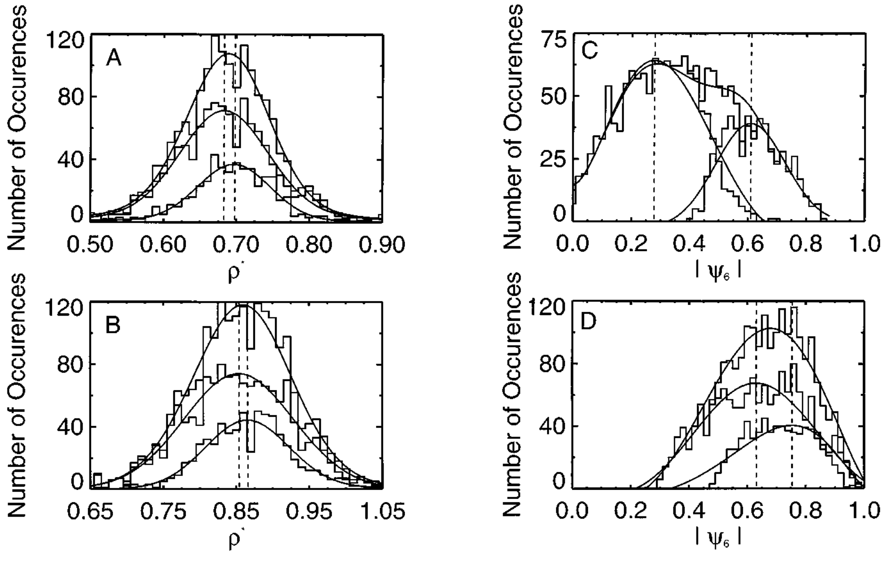

FIG. 15. Decomposition of local density (plots A and B) and bond orientation (plots C and D) distributions according to the analysis described in the text. An example of both liquid-hexatic ($\rho^*=0.693$, plots A and C) and hexatic-solid ($\rho^*=0.857$, plots B and D) densities are shown. The solid curves are best-fit Gaussian functions to the component distributions. Their peak positions (verticle dashed lines) and integrated areas give the values of the coexisting pure phase densities and the relative number of particles that occupy each phase. The complete results of our analysis are listed in Tables IV and V.

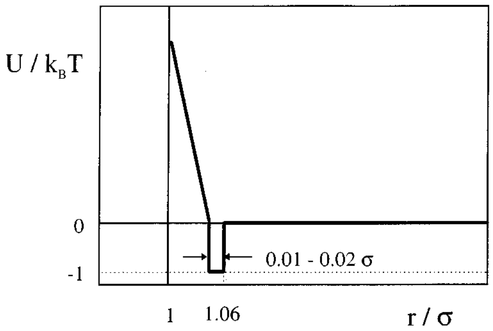

FIG. 16. Schematic representation of the pair potential conjectured to support a two-dimensional isostructural solid-solid phase transition. The attractive contribution occurs between 1.04σ and 1.06σ, and is due to a favorable enthalpic interaction between the segments of the brush polymers that coat the colloidal particles. At shorter interparticle separations, the polymer chains collapse, corresponding to a loss of configurational entropy and a rapid increase of the pair potential.

TABLE V. Lever rule analysis [see Eq. (5.7)] is the areal density; the A_i are the integrated areas of the Gaussian fits to the separate peaks in the local density distributions; the $l_i=|-_i|$ as described in the text. The subscript numbers indicate the peaks corresponding to the phases as identified in Table IV.

	A_1	A_2	l_1	l_2	n_2/n_1	l_1/l_2	% error
0.6887	11.961	4.510	0.0067	0.0153	0.377	0.438	14
0.6926	11.550	4.850	0.0096	0.0044	0.420	0.458	8
0.8459	12.630	7.610	0.0119	0.0201	0.602	0.592	1.7
0.8567	6.520	13.680	0.0037	0.0083	0.477	0.446	6.5

tive well located at about 1.06 particle diameters, a rapidly increasing repulsive interaction between 1.00 and, say, 1.04–1.05 particle diameters, and a hard core repulsion at 1.00 particle diameters. A cartoon representation of such a pair potential is shown in Fig. 16. A potential of this form has the qualitative features, and a range relative to the hard core repulsion, to support an isostructural solid-to-solid transition, if the parameters that define the potential have appropriate values. We conjecture that there is an as yet unobserved isostructural solid phase to solid phase in our system, and that the conditions under which our experiments have been conducted place the system in the domain where critical point fluctuations associated with the isostructural solid-to-solid phase transition drive the formation of the hexatic phase. Note, however, that the values of the parameters specific to our case are not known and no simulations which verify our conjecture have been carried out to date.

It is worth noting that in our experiments the medium in which the PMMA particles are suspended in an aqueous sucrose solution. We have considered the possibility that the solubility of the sucrose in the brush plus solvent immediately adjacent to the PMMA particle is different from that in

TABLE IV. Average values and standard deviations of order parameter distributions. The densities are those described in Table I. ρ is the local areal density [Eq. (3.5)], ψ_6 is the local bond orientational order parameter [Eq. (5.1)], and τ is the local correlation time given in units of sec [Eq. (5.2)].

	Thermodynamic state	$\langle\rho\rangle$	rms ρ	$\langle\psi_6\rangle$	rms ψ_6	$\langle\tau\rangle$	rms τ
0.011	dilute liquid	~	~	~	~	1.0	1.6
0.077	dilute liquid	0.176	0.076	0.285	0.192	3.0	2.1
0.241	dilute liquid	0.239	0.075	0.293	0.186	10.4	6.3
0.504	liquid	0.508	0.071	0.342	0.206	2.0	1.2
0.581	dense liquid	0.590	0.067	0.351	0.224	1.0	0.7
0.689	liquid-hexatic coexistence	0.692	0.066	0.420	0.306	4.31	2.1
	peak 1	0.682	0.068	0.277	0.240	4.24	1.98
	peak 2	0.704	0.059	0.608	0.123	4.47	2.30
0.693	liquid-hexatic coexistence	0.694	0.081	0.501	0.329	4.26	2.08
	peak 1	0.683	0.061	0.321	0.189	4.29	1.99
	peak 2	0.697	0.049	0.710	0.178	4.50	2.27
0.831	hexatic	0.833	0.071	0.62	0.316	5.21	3.1
0.846	hexatic-solid coexistence	0.850	0.064	0.665	0.201	11.44	5.4
	peak 1	0.834	0.067	0.630	0.193	11.39	6.1
	peak 2	0.866	0.052	0.753	0.188	11.58	5.2
0.857	hexatic-solid coexistence	0.859	0.068	0.688	0.225	11.61	5.8
	peak 1	0.853	0.076	0.635	0.218	11.44	6.2
	peak 2	0.865	0.058	0.751	0.222	11.65	5.5
0.874	solid	0.878	0.053	0.63	0.12	19.6	9.66
0.926	solid	0.932	0.042	0.65	0.23	95.7	31.9

the bulk medium, but have been unable to devise a scheme whereby this differential solubility, if it existed, would generate a free energy as a function of particle separation that resembles the functional form needed.

A comparison of the experiments that verify the predictions of the original KTHNY theory and the experiments reported in this paper, the simulations of Bladon and Frenkel and the analytic theory of Chou and Nelson, suggest an apparent richness of pathways associated with the melting transition in two dimensions. Although there are several known isostructural solid-solid phase transitions in three-dimensional systems, the melting transitions in those systems are not qualitatively different from melting in any other three-dimensional system. Indeed, the experimental evidence is that the melting transitions in all three-dimensional systems are first order, no matter what the potential energy function. In contrast, the pathway associated with two-dimensional melting does exhibit a dependence on the character of the intermolecular potential, as demonstrated by the difference between our results and those, for different systems, in which melting involves sequential continuous transitions. This apparent dependence of the melting pathway on the intermolecular potential in a two-dimensional system might be a signal of the nonuniversality of the two-dimensional melting transition, or it might result from restrictions on the regions of the thermodynamic parameter space available for realizable systems. The latter view is consistent with the results of Fisher and co-workers [35], who showed that a two-dimensional assembly of polarizable ions with allowed ion pairing has an insulating-to-conducting phase transition which is first order below a tricritical point, and of continuous Kosterlitz-Thouless type for temperatures above, and densities below, that tricritical point.

ACKNOWLEDGMENTS

Support for the research reported in this paper was provided by the Materials Science and Engineering Research Center at the University of Chicago, which is funded by the National Science Foundation through Grant No. DMR-9400379, and by National Science Foundation Grant No. CHE-9528923. We thank Professor David Grier for advice and technical assistance and Professor David Nelson for comments which deepened and improved our interpretation of the experimental results.

---

[1] For a review, see D. R. Nelson in *Phase Transitions and Critical Phenomena*, edited by C. Domb and J. L. Leibowitz (Academic, London, 1983), Vol. 7.

[2] J. M. Kosterlitz and D. J. Thouless, J. Phys. C **5**, L124 (1972); **6**, 1181 (1973).

[3] B. I. Halperin and D. R. Nelson, Phys. Rev. Lett. **41**, 121 (1978).

[4] D. R. Nelson and B. I. Halperin, Phys. Rev. B **19**, 2457 (1979).

[5] A. P. Young, Phys. Rev. B **19**, 1855 (1979).

[6] S. T. Chui, Phys. Rev. B **28**, 178 (1973).

[7] P. Bladon and D. Frenkel, Phys. Rev. Lett. **74**, 2519 (1995).

[8] T. Chou and D. R. Nelson, Phys. Rev. E **53**, 2560 (1996).

[9] V. M. Bedanov, G. V. Gadiyak, and Y. E. Lozovik, Phys. Lett. **92A**, 400 (1982).

[10] V. M. Bedanov, G. V. Gadiyak, and Y. E. Lozovik, Zh. Eksp. Teor. Fiz. **88**, 1622 (1985) [Sov. Phys. JETP **61**, 967 (1985)].

[11] K. J. Naidoo and J. Schnitker, J. Chem. Phys. **100**, 3114 (1994).

[12] H. Weber, D. Marx, and K. Binder, Phys. Rev. B **51**, 14 636 (1995).

[13] K. Bagchi, H. C. Anderson, and W. Swope, Phys. Rev. Lett. **76**, 255 (1996).

[14] M. A. Stan and A. J. Dahm, Phys. Rev. B **40**, 8995 (1989).

[15] For a review, see C. A. Murray, in *Bond Orientational Order in Condensed Matter Systems*, edited by K. J. Strandberg (Springer-Verlag, New York, 1992).

[16] T. Keyes and B. Ladanyi, J. Chem. Phys. **62**, 4787 (1975).

[17] G. Deville, A. Valdes, E. Y. Andrei, and F. I. B. Williams, Phys. Rev. Lett. **54**, 1710 (1985).

[18] D. C. Glattli, E. Y. Andrei, and F. I. B. Williams, Phys. Rev. Lett. **60**, 420 (1988).

[19] H. W. Jiang and A. J. Dahm, Surf. Sci. **229**, 352 (1990).

[20] C. A. Murray and D. H. Van Winkle, Phys. Rev. Lett. **58**, 1200 (1988).

[21] C. A. Murray and R. A. Wenk, Phys. Rev. Lett. **62**, 1643 (1989).

[22] C. A. Murray, W. O. Sprenger, and R. A. Wenk, Phys. Rev. B **42**, 688 (1990).

[23] A. J. Armstrong, R. C. Mockler, and W. J. O'Sullivan, J. Phys. Condens. Matter **1**, 1707 (1989).

[24] For a review, see K. J. Strandberg, Rev. Mod. Phys. **60**, 161 (1988); D. R. Nelson, Phase Transitions **7**, 1 (1983).

[25] A. Marcus, B. Lin, and S. A. Rice, Phys. Rev. E **53**, 1765 (1996).

[26] L. Antl, J. W. Goodwin, R. D. Hill, R. H. Ottewill, W. M. Owens, S. Papworth, and J. A. Waters, Colloid Surf. **17**, 67 (1986); K. E. J. Barrett, *Dispersion Polymerization in Organic Media* (Wiley, London, 1975).

[27] J. C. Crocker and D. G. Grier, J. Colloid Interface Sci. **179**, 298 (1996).

[28] R. Bruinsma, B. I. Halperin, and A. Zippelius, Phys. Rev. B **25**, 579 (1982).

[29] Y. Saito, Phys. Rev. B **26**, 6239 (1982); Phys. Rev. Lett. **48**, 1114 (1982).

[30] S. C. Davey, J. Budai, J. W. Goodby, R. Pindak, and D. E. Moncton, Phys. Rev. Lett. **53**, 2129 (1984). G. Aeppli and R. Bruinsma, *ibid.* **53**, 2133 (1984).

[31] J. Schofield, A. H. Marcus, and S. A. Rice, J. Phys. Chem. (to be published).

[32] A. E. Larsen and D. G. Grier, Phys. Rev. Lett. **76**, 3862 (1996).

[33] S. Berry, S. A. Rice, and J. Ross, *Physical Chemistry* (Wiley, New York, 1980).

[34] J. I. Martin and Z.-G. Wang, J. Phys. Chem. **99**, 2833 (1995).

[35] Y. Levin, X. Li, and M. E. Fisher, Phys. Rev. Lett. **73**, 2716 (1994); M. E. Fischer and Y. Levin, *ibid.* **71**, 3826 (1993).